Multi-Cycle Direct Numerical Simulations of a Laboratory Scale Engine: Evolution of the Momentum and Thermal Boundary Layers

Author(s):
Danciu, Bogdan A.; Frouzakis, Christos E.; Giannakopoulos, Georgios; Bode, Mathis

Publication date:
2023

Permanent link:
https://doi.org/10.3929/ethz-b-000676718

Funding acknowledgement:
952181 - Center of Excellence in Combustion (EC)

MULTI-CYCLE DIRECT NUMERICAL SIMULATIONS OF A LABORATORY SCALE ENGINE: EVOLUTION OF THE MOMENTUM AND THERMAL BOUNDARY LAYERS

***B.A. Danciu*[1], *C.E. Frouzakis*[1], *G.K. Giannakopoulos*[1], *M. Bode*[2]**

[1] ***CAPS Laboratory, Department of Mechanical and Process Engineering, ETH Zürich, 8092 Zürich, Switzerland***

[2] ***Jülich Supercomputing Centre, Forschungszentrum Jülich GmbH, 52425 Jülich, Germany***

danciub@ethz.ch

Abstract

Multi-cycle direct numerical simulations (DNS) of a laboratory-scale engine at technically relevant engine speeds (1500 and 2500 rpm) are performed to investigate the evolution of the momentum and thermal boundary layers (BL) under motored operation. The structure and behavior of engine BL is found to differ from canonical steady-state turbulent BL, requiring a more comprehensive understanding for the development of accurate predictive wall models in engineering simulations. The influence of the temporally-varying flow and the strong bulk motion in the cylinder on the BL is significant. Horizontal secondary flow vortical structures generated by the three-dimensional tumble flow are found to strongly influence the BL profiles as well as the evolution of wall heat flux, especially as the engine speed is increased. As a result, significant cyclic variability in the wall heat flux is observed, emphasizing the importance of near-wall phenomena in the overall engine performance.

1 Introduction

In the pursuit of reducing pollutant emissions and improving efficiency, current trends in internal combustion engines (ICE) involve strategies such as engine downsizing, turbocharging, and hybridization (Heywood 1988). Downsizing refers to the use of smaller cylinder volumes in combination with forced induction (turbocharging) or a hybrid powertrain, aiming to achieve improved performance with reduced environmental impact. A consequence of downsizing is the increase in the surface-to-volume ratio of the combustion chamber, which increases the significance of near-wall processes. Understanding the mechanisms of wall heat transfer and the evolution of thermal and momentum BL is therefore crucial for improving efficiency, reducing pollutant and unburned fuel emissions (Alkidas 1999), and selecting appropriate materials.

Experimental investigation of the near-wall region in ICE is challenged by limited accessibility. Traditional experimental methods, such as Laser Doppler Velocimetry (LDV) (Foster and Witze 1987) provide valuable insights, but have limitations in measuring velocities at discrete points. Particle Image Velocimetry (PIV) and Particle Tracking Velocimetry (PTV) have gradually replaced LDV, enabling the measurement of instantaneous two- or three-dimensional (2D or 3D) velocity fields close to the walls (Kähler et al. 2012). Alharbi et al. (2010) reported resolutions of up to $45\,\mu\mathrm{m}$ and the presence of sub-millimeter vortices within the BL. Jainski et al. (2013) studied the BL at the center of a pent roof-shaped cylinder head using a sum-of-correlation method with a resolution of $50\,\mu\mathrm{m}$. Renaud et al. (2018) further increased the wall-normal resolution up to $20\,\mu\mathrm{m}$. More recently, Schmidt et al. (2023) investigated the velocity BL above the piston by means of high-speed PTV with resolutions of up to $5\,\mu\mathrm{m}$ perpendicular to the wall. While these techniques have provided valuable data on the velocity BL in ICE, they are still limited to 2D slices or small volumes, providing only partial information.

The study of the thermal BL in ICE has also been challenging. Schlieren photography has been used to measure the thermal BL thickness in single-cylinder engines (Lyford-Pike et al. 1984). Coherent Anti-Stokes Raman scattering (CARS) has provided insights by measuring gas temperature and species concentrations (Kearney et al. 1999, Escofet-Martin et al. 2020, Ojo et al. 2021). However, the spatial resolution of CARS has limitations in accurately capturing the gas-phase temperature gradient at the wall.

To overcome the limitations of experimental techniques, DNS have emerged as powerful tools for investigating the BL in ICE (Schmitt et al. 2015, Giannakopoulos et al. 2023). By directly solving the Navier-Stokes equations without any modeling assumptions, DNS provide complete information on the evolution of velocity, temperature and composition. However, despite the significant progress in DNS for canonical flow configurations such as channel, stagnation or impinging flows (Hattori et al. 2004, Bradshaw and Hunag 1996, Son et al. 2016 and Ling et al. 2017), DNS of the entire ICE cylinder is scarce, especially at

high engine speeds, and only limited to single cycle realizations (Giannakopoulos et al. 2023).

This work aims to address the knowledge gap regarding the evolution of thermal and momentum BL and wall heat flux in ICE at relevant operating conditions by utilizing recent algorithmic and code developments, as well as state-of-the art GPU-based supercomputers. Building on the findings of previous studies by Schmitt et al. (2015) and Giannakopoulos et al. (2023), it focuses on a comprehensive investigation of the modified geometry of the pent-roof ICE studied experimentally at TU Darmstadt (TUDa) (Baum et al. 2014). The technically relevant full-load operating conditions at 1500 and 2500 rpm are considered, capturing the complex interactions between the in-cylinder flow and the engine walls. A total of 12 compression-expansion cycles for each operating condition was performed, enabling the acquisition of much needed phase-averaged statistics.

2 Numerical Methodology

The direct injection spark ignition engine of TUDa is a single, optically-accessible cylinder featuring a pent-roof, four-valve head design and an inlet duct designed to promote the formation of tumble flow. The cylinder of the square engine has a bore of $B = 86$ mm) typical of a passenger car engine. Detailed information regarding the engine and accompanying test facility can be found in the comprehensive work of Baum et al. (2014), while the engine operating conditions considered here are listed in Table 1. In comparison to the experimental engine geometry and to maintain the computational cost at affordable levels, the crevice volume was removed from the DNS domain. The bulk Reynolds number, defined as $Re = B\bar{V}_p/\nu$, where $\bar{V}_p$ is the mean piston speed, and ν the kinematic viscosity of air at the wall temperature and intake pressure, which is only indicative of the large-scale flow at the beginning of the compression stroke and varies with time, is 18,368 and 30,615 for the 1500 and 2500 rpm respectively, i.e. a 4.5 and 7.5-fold increase compared to the operating conditions of OP B simulated by Giannakopoulos et al. (2023).

The multi-cycle DNS was conducted using the spectral element solver NekRS (Fischer et al. 2022) developed at Argonne National Laboratory and extended for moving geometries at ETH Zurich. In addition to supporting CPU platforms, it is intended to work with GPU accelerated platforms using the

Engine speed	Intake press.	Re	OP
800 rpm	0.40 bar	4124	B
1500 rpm	0.95 bar	18368	C
2500 rpm	0.95 bar	30615	E

Table 1: Engine operating conditions. OP B simulated in Giannakopoulos et al. (2023) serves as a reference in this study and is not analyzed further.

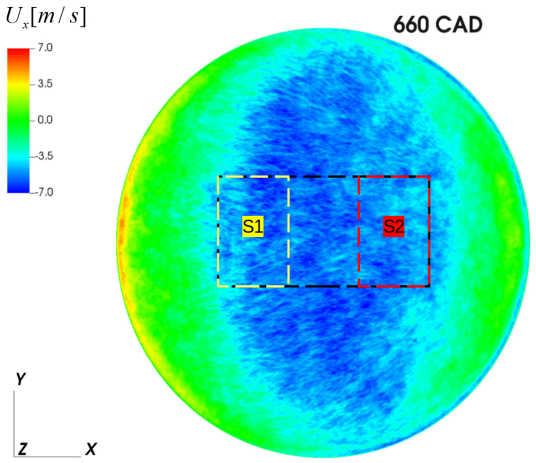

Figure 1: Favre-phase averaged wall-parallel velocity component 1 mm away from the piston surface at 60 CAD bTDC for OP C. The dashed black, yellow rectangle (S1) and the red rectangle (S2) mark the sampling regions discussed in the text.

portable Open Concurrent Computing Abstraction (OCCA) library (Medina et al. 2014), which allows for runtime code generation for different threading programming paradigms such as CUDA, HIP, OPENCL, and CPUs. This hybrid MPI+X parallelism approach enables seamless support for multiple hardware architectures.

The construction of computational grids that accurately represent complex ICE geometries poses a significant challenge for NekRS due to its requirement for conformal hexahedral meshes. The mesh generation using Coreform Cubit (Version 2022.11) involved initially filling the cylinder head volume with tetrahedral elements (TETs), which were then split into four hexahedrons (HEXs) each. The mesh of the lower horizontal plane of the cylinder head was subsequently extruded to the piston to create tensor product element layers capable of accommodating the vertical mesh deformation caused by piston motion while minimizing distortion. The arbitrary Lagrangian/Eulerian (ALE) formulation was used to account for the mesh deformation resulting from the piston motion. To ensure optimal resolution across the entire cycle, four grids with varying number of spectral elements were constructed, ranging from $E = 4.8$ to 9.3 million. This allowed to account for the increase in the flow Reynolds number and the reduction in turbulent scales during compression. Polynomial orders of $N = 7$ and $N = 9$ were chosen for the 1500 and 2500 rpm cases respectively, yielding meshes with 1.5 to 6.8 billion unique grid points. The mesh achieved an average resolution of 30 µm and 23 µm in the bulk, with the first grid point located 3.75 µm and 3 µm away from the wall for 1500 and 2500 rpm, respectively. To maintain high-order accuracy, scalable high-order spectral interpolation was employed to transition the solution from one

grid to the next.

The initial conditions for the simulations were obtained from precursor large eddy simulations (LES) validated statistically against available experimental data, as described in Giannakopoulos et al. (2023). Subsequent cycles were then selected from the LES results, and the data were interpolated onto the DNS grid at Intake Valve Closure at 600 crank angle degrees (CAD). The no-slip engine walls and the piston were considered isothermal at $T_w = 333$ K. Starting from initial conditions generated by means of LES, the low-Mach number form of the conservation equations were integrated in time with NekRS using a second-order semi-implicit scheme. The time step was adjusted dynamically during the simulation to maintain a fixed maximum Courant number of 2, ensuring numerical stability through the use of a high-order characteristics-based scheme (Patel et al. 2019). A total of 12 cycles were computed for each operating condition on JUWELS Booster GPU nodes at the Jülich Supercomputing Centre, each equipped with 2 AMD EPYC Rome CPUs (48 cores) and 4 NVDIA A100 GPUs. Simulations were performed on 70 and 130 GPU nodes for OP C and OP E, respectively. Based on the total number of CPU cores, 0.13 million core hours (Mcore-h) per cycle were required for OP C and 0.25 Mcore-h per cycle for OP E.

3 Results

Momentum and Thermal BL Evolution

A Favre-phase averaging technique was utilized for the 12 computed compression-expansion cycles in order to account for the density variation caused by the temperature disparity between the cold walls and the rising temperature in the bulk due to compression. In order to obtain better converged statistics, the Favre-phase averaging was combined with spatial averaging. In complex flow configurations such as that inside an ICE, determining the appropriate direction for spatial averaging is not readily apparent. Similarly to Giannakopoulos et al. (2023), the cross-tumble direction (i.e the direction parallel to the y-axis) was chosen, since it exhibits sufficient homogeneity as can be seen in the Favre-phase averaged wall-parallel velocity just above the piston shown in Fig. 1.

A domain covering a region of 4.5×3 cm^2 around the piston center was selected for the spatial averaging marked by the black dashed line in Fig. 1. In the following, the Favre-phase averaged $\tilde{u} =< \overline{\rho u}/\overline{\rho} >$ will be denoted as simply u. Inner scaling was used for all reported variables, with the scaled distance $z^+ = zu_\tau/\nu_w$, wall-parallel velocity $u^+ = u/u_\tau$, temperature $T^+ = \rho_w c_p(T_w - T)u_\tau/q_w$ with respect to the friction velocity $u_\tau = \sqrt{\tau_w/\rho_w}$, the wall shear stress $\tau_w = \sqrt{|\mathbf{T_w}|^2 - \sigma_w^2}$ where $\sigma_w = \mathbf{T_w} \cdot \mathbf{n}$ and the wall heat flux $q_w = \lambda_w \partial T/\partial n$; ρ_w, ν_w, λ_w, denote the density, kinematic viscosity, and thermal conductivity at the fixed wall temperature T_w, $\mathbf{n}$ is the unit vector normal to the piston surface, and $\sigma_w, \mathbf{T_w}$ the normal stress and traction vector at the wall.

The velocity and temperature profiles observed in Fig. 2 have comparable qualitative characteristics for the two operating conditions. In particular, the observed values for both profiles are in most of the cases lower than the predictions derived from the law of the wall, with the temperature profiles showing a greater deviation. While most conform to the linear velocity/temperature law for $z^+ \lesssim 5$, they do not clearly indicate the presence of a logarithmic layer region. This observation suggests an extensive convergence between the inner and outer layers, influenced by viscosity, as reported by Spalart (1988). It is also consistent with previous studies of BL structure in ICE (Renaud et al. 2018, Schmidt et al. 2023, Giannakopoulos et al. 2023).

Table 2 summarizes several parameters that characterize the BL computed in the sampling domain presented in Fig. 1. Both the velocity BL thickness defined by the wall distance of $0.99u_{xy,max}$ (Renaud et al. 2018), where $0.99u_{xy,max}$ is the magnitude based wall-parallel velocity, as well as the thermal displacement thickness δ_T as defined in Ojo et al. (2021) exhibit a consistent decrease throughout the compression stroke. The reduction in time can be attributed to the concurrent reduction in kinematic viscosity and turbulent length scales. The Re_θ (based on the momentum thickness θ, the maximum bulk velocity $u_{xy,max}$, and the viscosity at the wall), and displacement thickness δ^* values are low, although the BL display a turbulent behaviour. Confirmation of the turbulent character of the BL is supported by the observed values for the shape factor H, defined as the ratio between the δ^* and θ. In the context of laminar BL, the classical Blasius profile was found to have a shape factor of 2.59 (Schlichting and Kestin 1979). Conversely, turbulent BL at high Reynolds numbers have been found to have a shape factor that typically acquires values of about 1.4 (Schlichting and Kestin 1979). The values observed in this study are consistently less than 1.3, indicating that the configuration is consistent with a turbulent scenario, despite the relative low Re_θ. These observations indicate that the existence of a turbulent bulk flow leads to an accelerated onset of turbulence in the BL, consequently deviating from the anticipated characteristics of the BL as predicted by established theories.

Comparing the profiles for the two operating conditions shown in Fig. 2, it can be noted that the values for OP E (orange curves) are consistently slightly lower than the ones for OP C (blue curves), even though the Reynolds number is higher and the BL is expected to be more developed. To better understand this behaviour, the sampling domain is divided into three regions as shown in Fig. 1. The outer regions, labelled S1 and S2, are then subjected to further analysis and shown in Fig. 3.

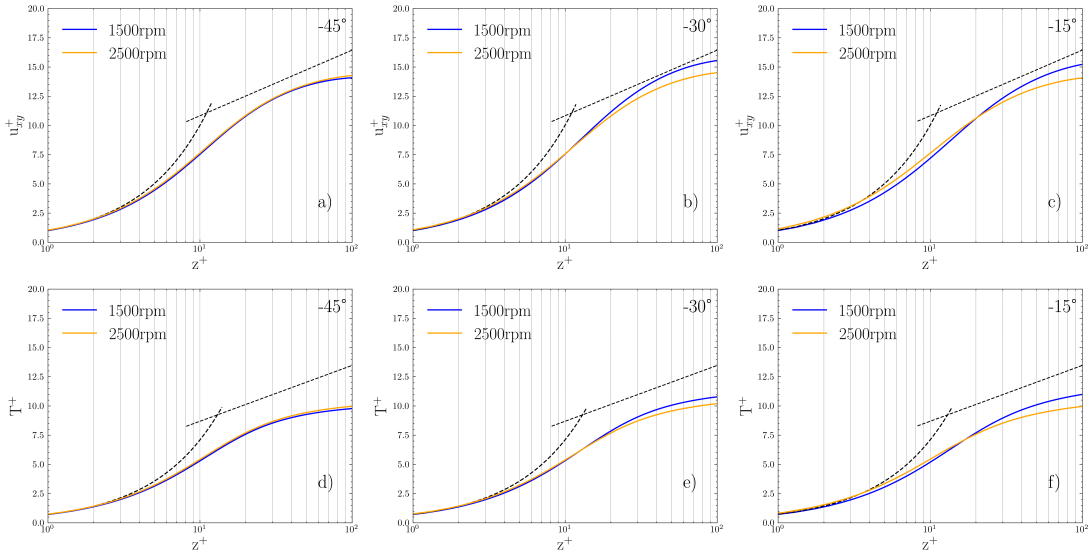

Figure 2: Scaled momentum and thermal boundary layers on the piston at 45, 30, and 15 CAD bTDC. Top row: magnitude-based wall-parallel velocity profiles; bottom row: temperature profiles;: black dashed lines law-of-the-wall profiles.

OP	CAD	δ [mm]	δ^* [mm]	θ [-]	H[-]	Re_θ [-]	δ_T [mm]
C	-45	0.77	0.07	0.06	1.26	82.52	0.14
	-30	0.66	0.05	0.05	1.08	101.51	0.13
	-15	0.52	0.04	0.04	0.89	104.74	0.11
E	-45	0.58	0.05	0.04	1.21	92.77	0.1
	-30	0.47	0.03	0.03	1.02	94.4	0.09
	-15	0.42	0.03	0.03	0.8	90.58	0.08

Table 2: Boundary layer parameters computed for OP C and E.

In region S2, the flow experiences an adverse (positive) pressure gradient as the tumble vortex impinges on the piston surface, which results in lower u^+_{xy} during earlier stages of compression. As the flow develops in time, a favorable (negative) pressure gradient is noted in this region, which corresponds to profiles progressively approaching developed wall jets, leading to higher values of u^+_{xy}. The profile values for OP E are higher than OP C, a characteristic of a more developed BL consistent with previous studies (Schmidt et al. 2023 and Giannakopoulos et al. 2023). However, in the S1 region, the velocity profiles for OP E show significantly lower values that continue to decrease as compression evolves, indicating an adverse (positive) pressure gradient suggesting flow deceleration. To understand this behaviour, it is necessary to study the phenomenology of the large-scale motion inside the cylinder in more detail.

As observed by Voisine et al (2011), the flow induced by the 3D tumble motion rolls up along the cylinder wall and concentrates in the centre of the upper region of the cylinder, creating two secondary horizontal vortex structures. These structures pertain primarily to the 3D advancement of the tumbling flow, rather than being indicative of its breakdown. They persist throughout the compression stroke and, as the piston approaches TDC, their influence on the piston BL becomes increasingly apparent, especially at higher engine speeds. As can be seen in Fig. 4, the velocity vectors confirm the presence of such structures (see left half of the piston surface), which induce a jet with a direction opposite to the one generated by the tumble flow. As a result, the flow decelerates and an adverse pressure gradient is introduced along the stream-wise direction. At the highest engine speed investigated, the influence of these vortex structures extends beyond the centre of the piston and significantly alters the BL profiles during the later stages of compression. Thus, compliance with the law of the wall in BL profiles depends strongly on the horizontal position and temporal evolution, as well as on the local flow structures that develop under different operating conditions.

Wall Heat Flux

The distribution of the average heat flux over different regions of the engine is shown in Fig. 6 for the

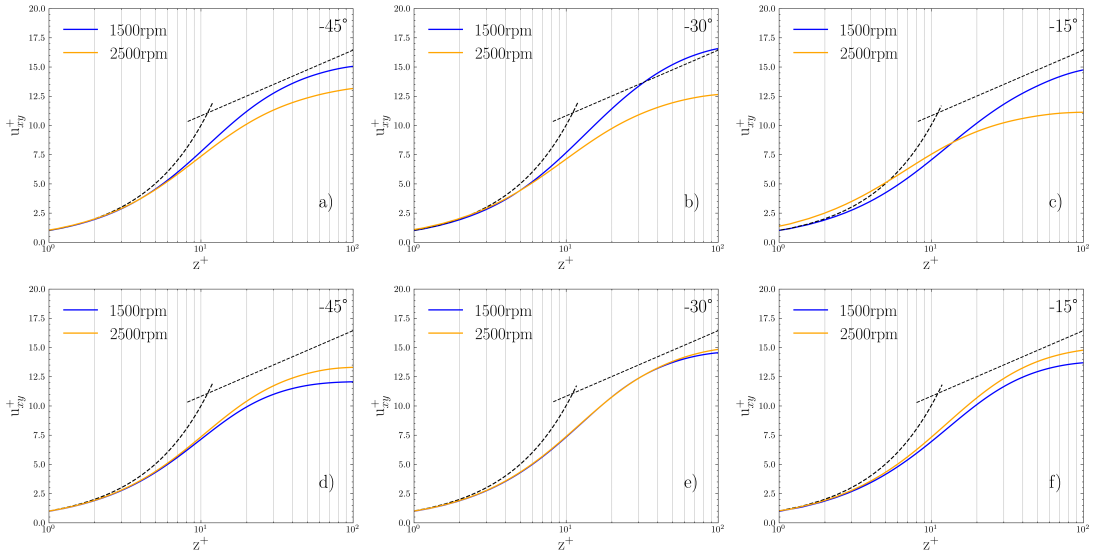

Figure 3: Scaled momentum boundary layers on the piston at 45, 30, and 15 CAD bTDC: magnitude-based processed wall-parallel velocity profiles for sampling domains S1 (top) and S2 (bottom); black dashed lines: law-of-the-wall profiles.

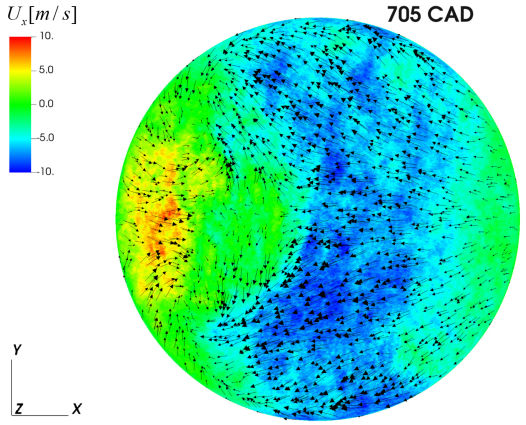

Figure 4: Favre-phase averaged wall-parallel velocity component 1 mm away from the piston with velocity vectors superimposed at 15 CAD bTDC for OP E.

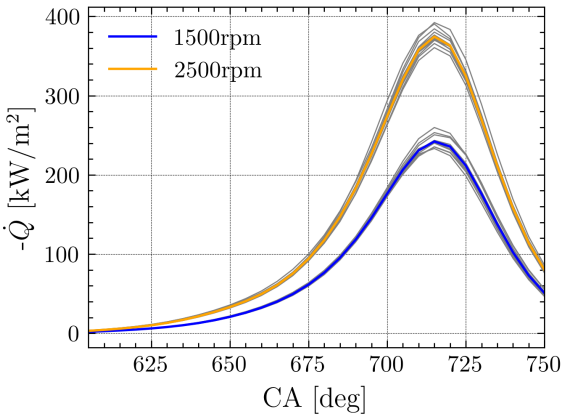

Figure 5: Surface-averaged heat flux along the cylinder walls during compression. Colored lines: average values, grey lines: individual cycles.

two operating conditions at 15CAD bTDC. On the left side of the cylinder head (Fig. 6, top row), where the flow impinges/stagnates due to tumbling motion, the average heat flux values are higher than on the right side, in agreement with previous studies (Schmitt et al. 2015 and Giannakopoulos et. al 2023). However, the distribution of heat flux on the piston differs between the two operating conditions and also from the results in Giannakopoulos et al. (2023). The highest values of OP C are observed more on the right side and in the centre of the piston, while OP E shows its highest values mainly in the middle left part. This could be an effect of the horizontal vortex structures shown in Fig. 4 converging and interacting in this region above the piston, impinging on the surface, as well as a shift of the tumble core to the left.

In terms of global metrics, the crank-angle resolved surface-averaged heat flux depicted in Fig. 5 peaks at TDC, as expected since this is the moment of peak cylinder pressure/temperature. More importantly, significant cycle-to-cycle variability of up to 8% is observed for both operating conditions, even though no combustion was considered.

4 Conclusions

Multi-cycle DNS of a laboratory-scale engine were performed at the technically relevant engine speeds of 1500 and 2500 rpm under full-load motored operation. The results confirm previous experimental and numerical findings that boundary layers in IC engines differ from idealized steady-state turbulent boundary layers, conditions that are commonly assumed in deriving scaling laws for wall model closures.

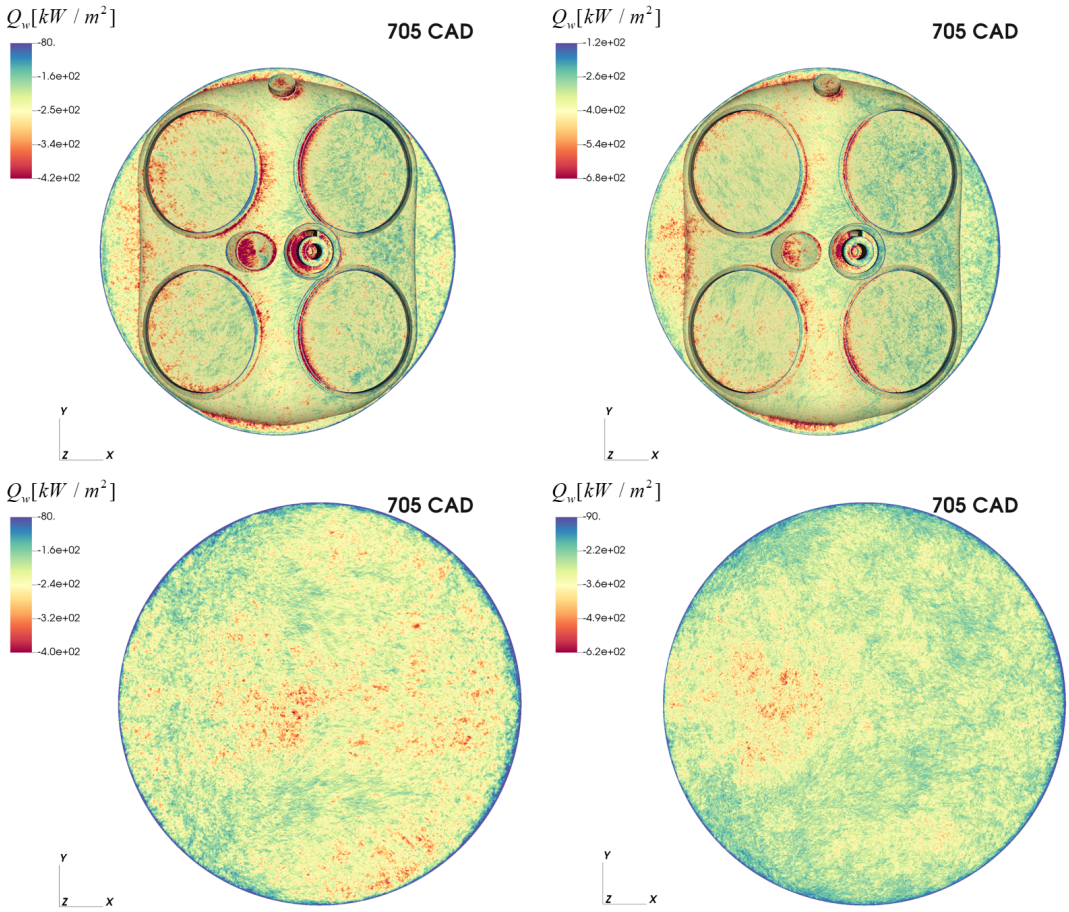

Figure 6: Iso-contours of the average heat flux at the cylinder walls for OP C (left) and OP E (right) at 15 CAD bTDC. Cylinder head view in the middle, and piston view at the bottom.

Understanding the temporal evolution of the flow and the influence of the strong bulk motion in the cylinder, as well as of local flow structures, is essential for accurate wall prediction models in engineering CFD. In addition to the inherent complexity of a time-varying wall-bounded flow, the coherent 3D tumble flow in pent-roof cylinder head engines generates horizontal secondary vortex structures that significantly affect boundary layer profiles and wall heat flux, especially at higher engine speeds. Significant cyclic variations in wall heat flux highlights the critical role of wall-related phenomena in overall engine performance. These results call for a comprehensive understanding of engine boundary layers and their dynamics to optimize engine efficiency and performance.

Acknowledgments

This project received funding from the European Union's Horizon 2020 research and innovation program under the Center of Excellence in Combustion (CoEC) project, grant agreement No 952181. The authors gratefully acknowledge the Gauss Centre for Supercomputing e.V. (`www.gauss-centre.eu`) for funding this project by providing computing time on the GCS Supercomputer JUWELS at Julich Supercomputing Centre (JSC) under the Multi-scale Data-driven Engine Modeling Using Direct Numerical Simulations (DEMS) project.

References

Alharbi, A. Y. (2010), Planar velocity measurements in an internal combustion engine using particle image velocimetry. *Int. J. Engine Res.*, 11(4), 309–326.

Alkidas, A.C. (1999), Combustion-chamber crevices: the major source of engine-out hydrocarbon emissions under fully warmed conditions, *Prog. Energy Combust. Sci.*, 25 (3), pp. 253-273.

Baum E., Peterson B., Böhm B., Dreizler A. (2014), On The Validation of LES Applied to Internal Combustion Engine Flows: Part 1: Comprehensive Experimental Database, *Flow, Turb. Combust.*, 92, 269–297.

Bradshaw, P., Huang, P. G. (1996). Turbulent boundary-layer structure in complex flows, *J. Fluid Mech.*, 322, 209–223.

Escofet-Martin, D., Ojo, A.O., Collins, J., Mecker, N.T., Linne, M., Peterson B. (2020), Dual-probe 1D hybrid fs/ps rotational CARS for simultaneous single-shot temperature, pressure, and O2/N2 measurements *Opt. Lett., 45*, pp. 4758-4761.

Fischer P., Kerkemeier S., Min M., Lan Y.-H., Phillips M., Rathnayake T., Merzari E., Tomboulides A., Karakus A., Chalmers N., Warburton T. (2022), NekRS, a GPU-Accelerated Spectral Element Navier-Stokes Solver, *Parallel Comput.*, 114, 102982.

Foster, D. and Witze, P. (1987), Velocity Measurements in the Wall Boundary Layer of a Spark-Ignited Research Engine, SAE Technical Paper 872105.

Giannakopoulos G.K., Keskinen K., Koch J., Frouzakis C. E., Y. Wright Y, Boulouchos K. (2023), Characterizing the Evolution of Boundary Layers in IC Engines by Combined Direct Numerical and Large-Eddy Simulations. *Flow Turb. Combust.* 110, 209–238.

Hattori, Y., Nagano, Y. (2004). Direct numerical simulation of turbulent heat transfer in plane impinging jet, *Int. J. Heat Fluid Flow*, 26(6), 933–947.

Heywood, J. B. (1988), Internal Combustion Engine Fundamentals. McGraw-Hill.

[6] Jainski C., Lu L., Dreizler A., Sick V. (2013), High-speed micro particle image velocimetry studies of boundary-layer flows in a direct-injection engine, *Int. J. Engine Res.*, 14 (3), pp. 247–259.

Kähler, C.J., Scharnowski, S., Cierpka, C. (2012), On the uncertainty of digital PIV and PTV near walls. *Exp. Fluids 52*, 1641–1656.

Kearney, S.P., Lucht, R.P., Jacobi A.M. (1999), Temperature measurements in convective heat transfer flows using dual-broadband, pure-rotational coherent anti-Stokes Raman spectroscopy (CARS) *Exp. Therm. Fluid Sci.*, 19, pp. 13-26.

Ling, S., Hoi, C. K., Zare-Behtash, H., Kontis, K. (2017). Direct numerical simulation of heat transfer characteristics in an impinging jet flow, *Int. J. Heat Mass Transfer*, 106, 207–223.

Lyford-Pike, E. G., Heywood, J. B. (1984), Structure of the thermal boundary layer in the transition region of an internal combustion engine. Combust. Sci. Techn., 40(3-4), 193–204.

Medina D. S., St-Cyr A., Warburton T. (2014), OCCA: A unified approach to multi-threading languages, *arXiv preprint arXiv:1403.0968*.

Patel, S., Fischer, P., Min, M., Tomboulides, A. (2019). A characteristic-based spectral element method for moving-domain problems. *Journal of Scientific Computing*, 79(1), 564-592.

Renaud, A., Ding, C.-P., Jakirlic, S., Dreizler, A., and Böhm, B. (2018), Experimental characterization of the velocity boundary layer in a motored IC engine, *Int. J. of Heat and Fluid Flow*, 71, p 366-377.

Schmidt M., Welch C., Illmann L., Dreizler A., Böhm B. (2023), High-speed measurements and conditional analysis of boundary-layer flows at engine speeds up to 2500 rpm in a motored IC engine, *Proc. Combust. Inst.*, 39(4), 4841–4850.

Schmitt, M., Frouzakis, C.E., Tomboulides, A.G., Wright, Y.M., Boulouchos, K. (2015), Direct numerical simulation of the compression stroke under engine-relevant conditions: evolution of the velocity and thermal boundary layers, *Int. J. Heat Mass Transf.* 91, 948–960.

Schlichting, H. and Kestin, J. (1979), Boundary-layer theory (7th ed.), McGraw-Hill, New York and London.

Son, S., Moin, P., Moser, R. (2016). Direct numerical simulation of a fully turbulent square jet impinging on a flat plate, *Journal of Fluid Mechanics*, 804, 23–69.

Spalart, P., (1988). Direct simulation of a turbulent boundary layer up to Reθ = 1410, *J. Fluid Mech.*, 187, pp. 61-98.

Ojo, A., Escofet-Martin, D., Collins, J., Falconetti, G., Peterson, B. (2021), Experimental investigation of thermal boundary layers and associated heat loss for transient engine-relevant processes using HRCARS and phosphor thermometry, *Combustion and Flame*, 233, 111567.

Voisine, M., Thomas, L., Borée, J. et al. (2011), Spatio-temporal structure and cycle to cycle variations of an in-cylinder tumbling flow, *Exp Fluids* 50, 1393–1407.